Applied Thermal Engineering 148 (2019) 129–135

Contents lists available at ScienceDirect

Applied Thermal Engineering

journal homepage: www.elsevier.com/locate/apthermeng

Simulation on tip-assisted focusing of laser energy for sub-surface photon heating

Yixin Chen[a], Yanru Xu[a], Danmei Xie[a,*], Jin Jiang[a], Yanan Yue[a,b,*]

[a] Key Laboratory of Hydraulic Machinery Transients (MOE), School of Power and Mechanical Engineering, Wuhan University, Wuhan, Hubei 430072, China
[b] Department of Mechanical Engineering, Boston University, Boston, MA 02215, USA

A B S T R A C T

The extensive confinement of electromagnetic field and the resulting localized heating effect induced by metallic nanotips are of great interest which promise novel applications including material surface processing and laser-assisted manufacturing. In this work, the sub-surface heating effect of silicon and monolayer graphene induced by gold nanotip-light interaction is studied through numerical simulations. The optimized optical enhancement around a free-standing gold tip is firstly studied with respect to the incident laser wavelength and incident angle. The maximum electric intensity enhancement is up to ~66 times within sub-10 nm region around the tip apex which is obtained under a 532 nm p-polarized laser incidence. With the presence of silicon under the nanotip, the optical field in the gap is enhanced further, generating a heat source at the sub-surface (~2 nm depth) of silicon. The heat source energy density is as high as 3×10^{15} W m^{-3} with a moderate incident intensity of 2×10^{7} W m^{-2}. As for gold nanotip-monolayer graphene configuration with a separation distance of 1 nm, the enhanced electric field can penetrate into monolayer carbon atoms and induce intensive heating by 55 times in the graphene and by 10^{4} times across the carbon layer surface, which could be used for localized modifications of graphene surface like surface cleaning and property tuning. Simulation results in this work provide a guide for the laser-assisted manufacturing/modification not only in the bulk materials but also in the 2D nanostructures.

1. Introduction

The ability of concentrating electromagnetic field down to a sub-diffraction region makes metallic nanostructures, such as nanorods, nanoparticles and nanotips, attract much attention [1]. Among them, metallic nanotips can produce stronger field localization around the tip apex [2,3], which has been applied to improve optical processes in numerous fields, including materials characterization [4], surface imaging [3], and biological sensing [2,4]. The extremely high confinement of optical field generated by metal nanotip is primarily attributed to the implement of surface plasmon polaritons (SPPs) [2,4], which originate from the collective oscillations of the surface electron gas at the metallic-dielectric interfaces. Due to the resulting localized surface plasmon resonance (LSPR) [5,6] and the lightning-rod effect [5,7,8], the optical field near the interface between the metal and dielectric medium is significantly enhanced.

In the past, many efforts have been made to study the nanotip-induced optical enhancement through theoretical [8,9], numerical [8,10] and experimental [10,11])approaches. The localized optical field (also called hot spot) is usually found generated by the Au and Ag nanotips under external visible illumination. It is attributed to the negative permittivity of noble metals in visible range, which contributes to generation of SPPs [2]. The local field enhancement is also found closely related to the tip geometry including tip shape, radius, length and cone angle, which have been systematically studied [2,11–13]. Up to now, the tip-induced field enhancement effect has been extensively studied, however, the resulted thermal effect upon the tip-related structures is still lacking, which is desirable in terms of thermal energy-related applications, such as tip-assisted manufacturing. There is considerable room for understanding the light-material interactions under such extreme condition.

In the illuminated tip nanostructures, the resulting thermal effects via Joule heating due to the enhanced light absorption may be detrimental to the tip and sample materials or lower the optical signal. Chen et al. numerically studied the near-field thermal transport in a tungsten nanotip on a silicon substrate under pulse laser irradiation [14]. They found that the field enhancement induced heating effect at the tip apex is related to the taper angle and tip radius. Downes et al. numerically confirmed that the significant heating effect around tip apex was due to the tip-substrate cavity induced field enhancement through comparing that with the case without a tip present [15]. Zhang et al. experimentally observed the morphological changing of the underneath Au surface and the Raman signal loss from the surface covered indicators. Their numerical simulation implied that it was due to the annealing effect resulting from the tip-substrate cavity induced near-field heating [16]. Datta et al. numerically designed and optimized a plasmonic

* Corresponding authors at: Key Laboratory of Hydraulic Machinery Transients (MOE), School of Power and Mechanical Engineering, Wuhan University, Wuhan, Hubei 430072, China (Y. Yue).
E-mail addresses: dmxie@whu.edu.cn (D. Xie), yyue@whu.edu.cn (Y. Yue).

https://doi.org/10.1016/j.applthermaleng.2018.11.050
Received 27 April 2018; Received in revised form 7 November 2018; Accepted 13 November 2018
Available online 13 November 2018
1359-4311/

nanoantenna for inducing near-field heating which was employed in the magnetic writing [17].

Apart from the above studies, our group has also previously investigated the tip-induced temperature rise in the underneath silicon sample through experiments [18]. However, the detailed understanding of the optical-thermal energy conversion process in near field is still lacking due to the difficulty and complexity of experiments at nanoscale. Other than bulk materials, studies on the localized heating of 2D materials may also be attractive and useful which promises new applications such as material properties tuning. Wei et al. achieved tuning the reduction of graphene oxide (GO) by localized heating with dimensions down to 12 nm using a heated AFM tip [19]. The nanotip-2D materials configuration may provide opportunity for functional properties tuning and surface morphology modifications via the near-field heating.

In this work, a gold nanotip is used to confine the incident light to enhance the photo-thermal energy conversion in silicon and monolayer graphene. Finite element method (FEM) simulations are performed to study the optical confinement induced by a free-standing gold nanotip under different incident angles and typical incident wavelengths. The light concentration effect induced by the gold nanotip-silicon cavity and the corresponding optical-thermal energy conversion process are then calculated. Finally, monolayer graphene is selected to study the optical enhancement distribution in nanotip-2D material configuration at different gap separations as well as the related energy conversion.

2. Modeling details

To simulate the optical field distribution around the free-standing nanotip and the nanotip-substrate configuration, three-dimensional models are built based on FEM, which is an effective tool for solving Maxwell's equations for complex near-field light-matter interactions thanks to the unique meshing advantages. The schematic view for the symmetric cross-section of free-standing nanotip is shown in Fig. 1(a). Based on the previous results of the effects of tip geometries on the optical enhancement [11,12,20], a tapered conical tip with half cone angle $\alpha = 10^{\circ}$ whose sharp end is tangential to a hemisphere of $R = 30$ nm is used throughout our simulation. The total length of the tip is fixed at $L = 200$ nm. The tip is illuminated by a p-polarized incident wave from one side with an incident angle θ (the angle between the wavevector and the x-axis) and wavelength λ. For simplicity, the amplitude of electric field is set as $E_0 = 1\ \mathrm{V\,m^{-1}}$.

To reduce the computational and memory cost, only half of the whole domain is calculated, as the configuration is symmetric with respect to the conical axis. The symmetry plane is modeled as $\mathbf{n} \times \mathbf{H} = 0$ such that the tangential magnetic field and the surface current density are 0, which ensure electric fields being symmetrical. The reduced computational domain is built as $Lx \times Ly \times Lz = 1200\ \mathrm{nm} \times 600\ \mathrm{nm} \times 1200\ \mathrm{nm}$, surrounded by a 100 nm-thick perfectly matched layer (PML) which is used to prevent the light reflection from the outer boundaries. The whole computing domain is divided into more than 4×10^5 unstructured mesh elements. In the near-field region with complex geometries containing the tip apex and the substrate, the mesh elements are adaptively refined, ensuring them small enough to maintain the calculation accuracy. Mesh independent study has been conducted to ensure that meshing is irrelative to the simulation results.

To achieve noticeable energy localization, the tip-induced optical enhancement resulting from the surface plasmons should be strong, while the light absorption by the tip itself is ideally minimal. This requires the permittivity of the tip material with low negative real part and low imaginary part. Among the common plasmonic materials including silver, gold, copper and aluminum, gold is a preference choice for the tip material due to its chemical stability and the support of surface plasmons in the near-infrared (NIR) range. The material optical properties are derived from Palik's handbook [21] and Aspnes and

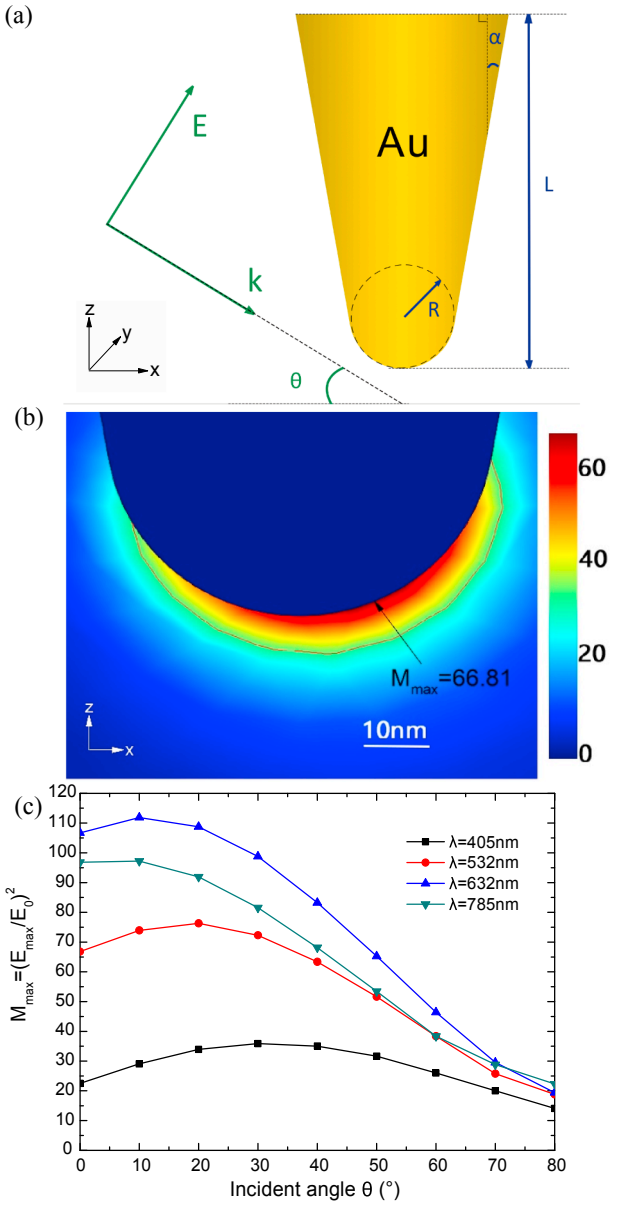

Fig. 1. (a) Schematic of Au tip at the symmetric cross section with the fixed geometry: tip radius $R = 30$ nm, half cone angle $\alpha = 10^{\circ}$ and tip length $L = 200$ nm. (b) Distribution of the optical enhancement factor M_{loc} around the tip apex at $\lambda = 532$ nm and $\theta = 0^{\circ}$. (c) Dependence of M_{max} on the incident angle θ and wavelength λ (405 nm, 532 nm, 632 nm, and 785 nm).

Studna's work [22]. The relative permittivity of gold at 405 nm, 532 nm, 632 nm, and 785 nm is -1.0678 + 5.6096i, -4.2854 + 2.3292i, -10.510 + 1.2784i, and -21.008 + 1.6846i, respectively. The relative permittivity of Si at 532 nm is 17.237 + 0.43004i. The electrical conductivity of gold and silicon are 4.1×10^7 S/m and 1.0×10^{-12} S/m, respectively.

3. Simulation results and discussion

3.1. Optical concentration by Au tip

The electric intensity enhancement (M_{loc}) distribution around the Au nanotip is firstly discussed. $M_{\mathrm{loc}} = I_{\mathrm{loc}}/I_0 = (E_{\mathrm{loc}}/E_0)^2$ is used to illustrate the local intensity enhancement factor in the system. Here, I_{loc} denotes the local optical intensity ($I = 0.5 n \varepsilon c_0 E_{\mathrm{loc}}{}^2$). The electric field term E_{loc} is directly calculated from the Maxwell's equations. Fig. 1(b)

shows the cross section of the M_{loc} distribution in the near-field region at $\lambda = 532$ nm (commonly used in experiments) and $\theta = 0°$. The strong optical enhancement distributes in the vicinity of the tip apex, as the sharp Au tip functions as an optical antenna. The maximum intensity enhancement M_{max} is 66.81 at $\lambda = 532$ nm. The optical enhancement peaks at the surface of the tip apex and decays outwards gradually. The decay ($M_{loc} < M_{max}/2$) occurs over ~10 nm far from the tip surface, as denoted by the red line. Our used tip can concentrate the incident energy into 10 nm region around the tip apex. The concentration mainly distributes at the back of the tip apex with respect to the incident direction. The enhancement peak shifting to the back side is due to the asymmetric illumination with respect to the cone axis [10,13,14].

The effect of incident wavelength λ and incident angle θ on M_{max} is then analyzed. The maximum intensity enhancement for four typically-used λ (405 nm, 532 nm, 632 nm, and 785 nm) and nine θ (0° ~ 80°) are shown in Fig. 1(c). Among the calculated results at the four wavelengths, the largest M_{max} at all incident angles occurs at the red incidence (632 nm). The calculated M_{max} at 632 nm is comparable to the numerical result obtained by Zhang et al. for the gold tip with similar parameters [20]. Moreover, it approximates to the previous theoretical calculations results ($M_{max} = 144$) for a gold tip with $R = 30$ nm and $\theta = 10°$ at 635 nm incidence, despite the slight difference arising from the tip length and computational method [23]. The optical enhancement at 632 nm and 785 nm higher than that at 405 nm is due to that gold permittivity has higher absolute value of the negative real part $|\mathrm{Re}(\varepsilon)|$ at red and near-infrared regime while $|\mathrm{Re}(\varepsilon)|$ at 405 nm is relatively low [2]. The strongest field enhancement yields at 632 nm is due to that the incident wavelength is close to the surface plasmon resonant frequency. It is revealed that besides the tip geometries, the optical enhancement varies with incident features [11,12,20]. The most commonly accepted related interpretations are the two main mechanisms, LSPR [4,6] and the lightning-rod effect [7,8,20]. The excitation of LSPR arises from the collective oscillation of the localized surface electrons of the tip apex, which is correlated to the dielectric constant of the material at the incident frequency. The lightning-rod effect is a shape-related effect that occurs at the singular pints of the metallic structure especially the tip end.

3.2. Sub-surface absorption in silicon

The schematic view for the symmetric cross-section of the Au tip-silicon configuration is illustrated in Fig. 2. The separation between tip and silicon is denoted as d and the silicon upper surface defines the x-y plane. The illumination is fixed at $\lambda = 532$ nm and $\theta = 0°$. As d is in the nanoscale, the optical field in the gap region in-between is significantly enhanced, as shown in Fig. 3(a). The intensity enhancement is induced not only by the tip itself, but also by the substrate and the extremely tiny gap [5]. From the discussion in the above section, it is known that without the presence of the substrate ($d = \infty$), M_{max} is 66.81 at 532 nm. With the presence of the substrate, M_{max} increases to 136 at $d = 10$ nm. As d is decreased from 10 nm to 1 nm, M_{max} gradually increases [10,14]. As d continues to drop from 1 nm until to the tip contacting the substrate, M_{max} increases exponentially and finally reaches its maximum value when the tip contacts the substrate [2]. The inset of Fig. 3 (a) illustrates the M_{loc} (on a log scale) distribution in the near-field region in the contacting case. A high enhancement factor $M_{max} = 5.5 \times 10^4$ is obtained around the tip apex.

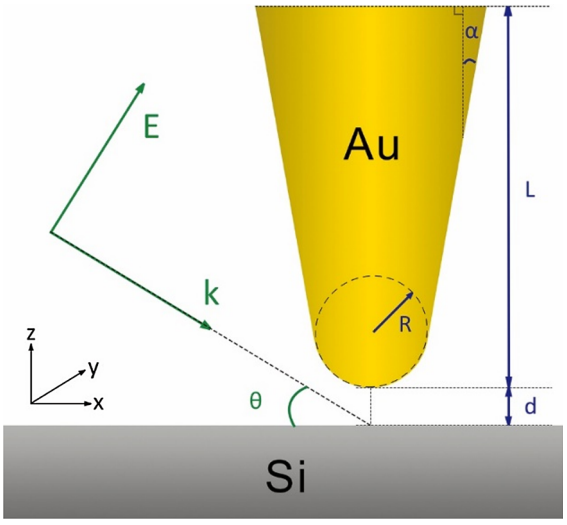

Fig. 2. Schematic of the tip-silicon configuration with a separation d illuminated by a fixed incidence: $\lambda = 532$ nm and $\theta = 0°$.

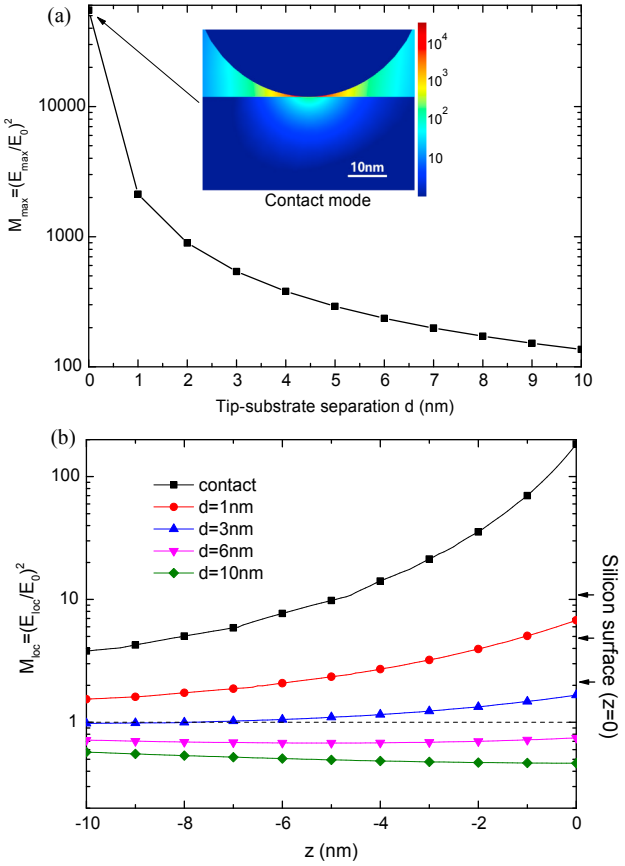

Fig. 3. (a) The variation of the maximum optical enhancement M_{max} in the Au tip-Si configuration with respect to the separation d. The inset shows the optical enhancement M_{loc} distribution on a log scale at the contacting configuration. (b) M_{loc} inside the silicon substrate along tip apex distributes on the z-axis.

Simultaneously, there is noticeable induced absorption of the concentrated electromagnetic radiation in the silicon, locating under the tip apex nearby the near-field region. The distribution of M_{loc} in the silicon is hemispherical, decreasing intensely from the surface towards the inside. The distributions of M_{loc} on the extension line of the cone axis along z- direction inside the silicon for different d are shown in Fig. 3(b), with $z = 0$ denoting the substrate surface. For each separation, the concentrated optical field penetrates from the sample surface to the inside part. In the contacting tip-silicon configuration M_{loc} on the substrate surface increases by 184 times with respect to the case of $d = 1$ nm, which can induce significant light absorption in the silicon, where a strongly enhanced range of $M_{loc} > M_{max}/2$ covers the depth of 1.8 nm from the silicon surface. For the case of $d = 6$ nm and $d = 10$ nm, there may be no noticeable light absorption since M_{loc} is all smaller than 1. As such, it should be pointed out that in real

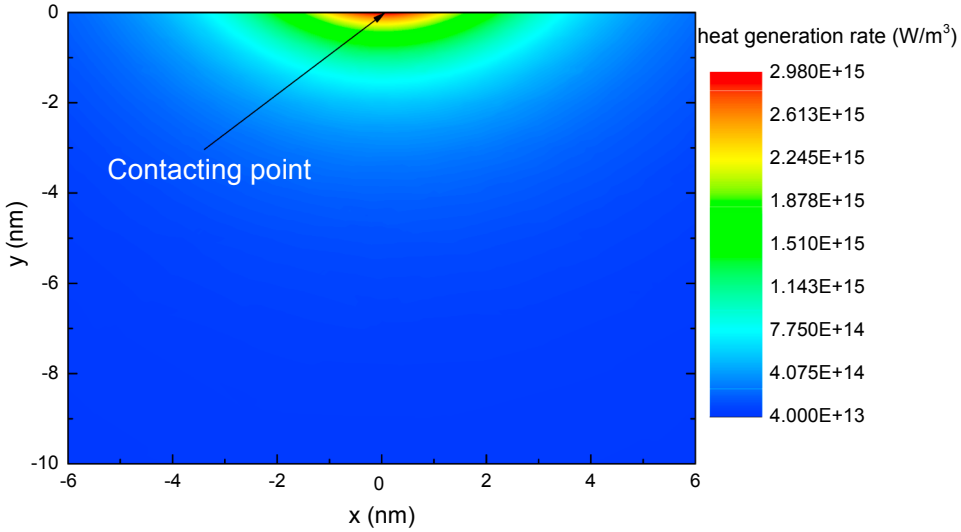

Fig. 4. The induced heat source q_{loc} distribution inside the bulk silicon for the contacting tip-sample configuration.

experiments, it is important to control the tip-substrate separation d for tuning the light absorption of substrate.

To study the heating effect induced by the local optical enhancement, the light absorption and the converted heat source distribution is calculated. A moderate incident intensity $I_0 = 2 \times 10^7\ \mathrm{W\,m^{-2}}$ is used for a rough calculation of the heat generation in the silicon, which is available in our laser equipment. The equivalent amplitude of incident electric filed is $E_0 = 1.2276 \times 10^5\ \mathrm{V\ m^{-1}}$ based on the equation of $I = 0.5n\varepsilon c_0 E^2$. Based on the Poynting's theorem [24], when light passes through the absorbing medium, the localized heat generation rate q_{loc} is described as $q_{loc} = 0.5\varepsilon_0\omega \mathrm{Im}[\varepsilon(\omega)]E_{loc}^{\ 2}$ [25,26], where ε_0 is the vacuum permittivity, ω is the angular frequency of the incident wave, Im $[\varepsilon(\omega)]$ is the imaginary part of the dielectric function of Si (known as the extinction coefficient) at the incident frequency and E_{loc} is the amplitude of the local electric field.

The heat generation rate q_{loc} (in $\mathrm{W\ m^{-3}}$) distribution inside silicon under the illuminated gold tip at the contacting configuration is shown in Fig. 4. The maximum induced energy density (or heat source) is as high as $q_{max} = 2.98 \times 10^{15}\ \mathrm{W\,m^{-3}}$ located at the contact point. q_{loc} distributes in a hemi-ellipsoidal region in accordance with the electric intensity enhancement distribution shown in the inset of Fig. 3(a). Towards the inside of the silicon, q_{loc} drops dramatically. The region of $q_{loc} > q_{max}/e$ covers a depth of 1.04 nm. The asymmetrical distribution along the x-axis is attributed to the asymmetrical distribution of tip-induced optical enhancement discussed in Section 3.1. Thus, the optical enhancement induced heat source in silicon is as small as ~6 nm laterally (along x-axis) and ~2 nm vertically (along z-axis).

The extremely small scale of the generated heat source in silicon here is sub-10 nm, smaller than the phonon mean free paths (MFPs) of bulk Si which is over 100 nm [27–29]. Thus, the scale relationship of heat source and the phonon MFPs determines that the heat dissipation from the hot spot will not follow the Fourier's law of thermal conduction because of the lack of enough scattering of phonons in a small volume to build the thermal equilibrium thermal equilibrium [27,30]. Our studied results provide a way to explore the quasi-ballistic thermal transport which promises new application, such as heat-assisted magnetic recording (HAMR). It employs the localized heating of the recording medium to achieve high density data recording [31]. The near-field heating can increase the localized temperature of recording material and decrease its coercivity which allows magnetic writing. Besides, the near-field effect can be used to induce subsurface heating of materials for target modification, such as laser-induced desorption, ionization and surface cleaning [32]. The controllable localized heating is also applicable for melting/removing materials. The laser induced periodic surface structures used for sub-diffraction limit writing has been achieved [33]. It is reported that silicon nanoparticles can also support optical heating with the help of the optical enhancement arising from the attaching Au nanoparticles [34], while the metallic tip with small tip apex in our study provides more localized near-field heating. Au nanoparticles can also achieve calibration-free nanothermometry utilizing the anti-Stokes luminescence emission spectra [35]. Temperature-feedback controllable direct laser-induced reshaping has been achieved on silicon nanorods with strong laser power [36]. Owing to the induced significant optical enhancement, the tip-assisted subsurface heating could also provide opportunities for application of controllable laser-induced writing in bulk materials for creating micro/nanostructures with features beyond the diffraction limit. A novel approach to generate broadband light emission by Si/Au nanoparticles system for nanospectroscopy has also been proposed [37], which utilized the near-field optical heating of the silicon nanoparticle enhanced by the Au nanoparticle.

3.3. Localized absorption in graphene

As a representative 2D material, the physical properties of graphene has been extensively studied, especially the thermal property. Due to the relatively large MFPs [38], the high thermal conductivity facilities the applications of graphene in many thermal management devices. The related issues about nanoscale thermal transport in graphene-based devices are attracting and need to be addressed. Besides, the fabrication process of graphene-based and other 2D materials-based devices requires the localized heating of the material for surface cleaning or material properties tuning. Thus, the laser-induced near-field heating provides opportunity for investigation of the nanoscale thermal transport as well as the localized modification of graphene. It has been reported that graphene can support the propagation of SPPs and provide opportunity for suitable alternative of noble metals [39]. Due to the atomic-thin structure, the strong interaction of light with graphene can yield light confinement and minimal energy loss [40–42]. Thus, it is feasible to employ the tip-graphene configurations to generate strong optical enhancement [43,44].

The schematic view for the symmetric cross-section of the Au tip-monolayer graphene configuration is illustrated in Fig. 5(a). The in-between gap separation is also denoted as d. The area of the monolayer graphene is set large enough to prevent the influence of the graphene edges on the electric field distribution. The incident light is fixed at λ = 532 nm and $\theta = 0°$, with $E_0 = 1\ \mathrm{V\,m^{-1}}$. In order to accurately solve the Maxwell's equations in the near field, the mesh elements in the near-

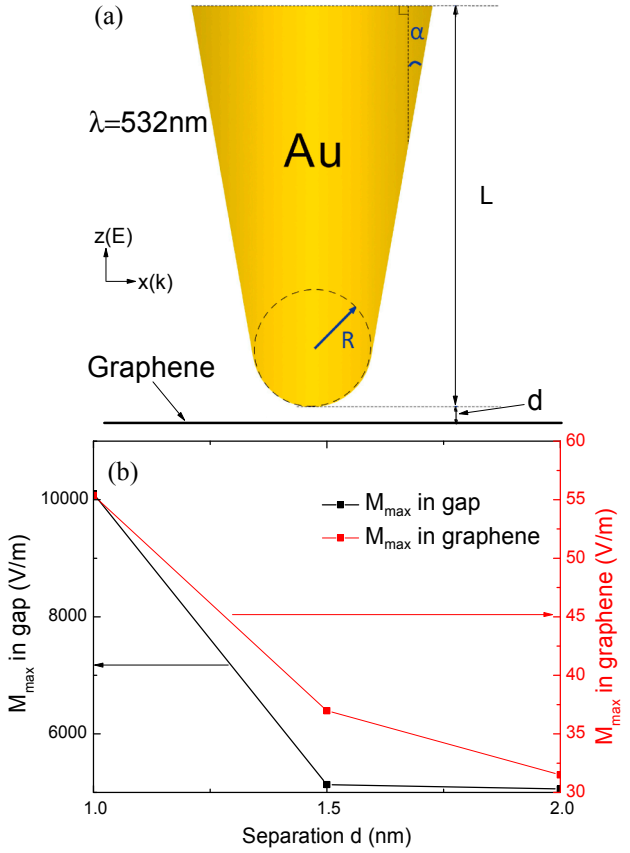

Fig. 5. (a) Schematic of the gold tip-monolayer graphene configuration. (b) The maximum optical enhancement M_{max} at different separations d. The black line denotes the M_{max} in the gap region while the red line denotes the M_{max} inside the monolayer graphene.

field region need careful handling. The domain representing the monolayer graphene is divided into structured mesh elements to improve the convergence, while the tip and the near-field surroundings are divided into extremely confined unstructured elements.

Different from most optical materials, the optical properties of atomic-thin graphene are usually represented in terms of the surface conductivity. At the visible range, considering the contributions of both the intraband and interband transition, using the random phase approximation (RPA) method, the surface conductivity of graphene is expressed as [39,45,46],

$$\sigma(\omega) = \frac{ie^2 k_B T}{\pi\hbar^2\left(\omega + \frac{i}{\tau}\right)}\left[\frac{E_F}{k_B T} + 2\ln\left(e^{-\frac{E_F}{k_B T}} + 1\right)\right] + \frac{ie^2}{4\pi\hbar}\ln\left[\frac{2E_F - (\omega + \frac{i}{\tau})\hbar}{2E_F + (\omega + \frac{i}{\tau})\hbar}\right] \quad (1)$$

where ω is the incident frequency, E_F is the energy of the Fermi level, e is the electron charge; $\hbar$ is the reduced Planck's constant; $\tau = 0.1$ ps is the relaxation time of the charge carriers; k_B is the Boltzmann constant; $T = 300$ K is a temperature. The electrical properties of graphene are controlled by E_F, which is fixed at $E_F = 0.4$ eV in this work. The dielectric function of the monolayer graphene is expressed as $\varepsilon(\omega) = 1 + i\sigma(\omega)/\varepsilon_0\omega t_g$[46], where ε_0 is the vacuum permittivity and $t_g = 0.34$ nm is the thickness of the monolayer graphene. With the determined dielectric functions and electrical conductivity, Maxwell's equations are solved among the whole domain.

The maximum optical enhancement $M_{max} = (E_{max}/E_0)^2$ in the gap and graphene at different d is shown in Fig. 5(b). The black and red line denotes M_{max} in the gap and graphene, respectively. As d is increased, both M_{max} decrease, which is similar to the tip-silicon case. At $d = 1$ nm, the maximum optical enhancement in the gap is stronger, with M_{max} over 1.0×10^4, compared with that ($M_{max} = 2122$) of the tip-silicon gap (see Fig. 4a). This is due to that the propagation of graphene SPPs contributes to the optical enhancement in tip-graphene gap. At $d = 1$ nm, the optical enhancement in the graphene is also enhanced significantly, with $M_{max} = 55$, larger than that of tip-silicon case. The light absorption in the monolayer graphene can also be calculated using $q_{loc} = 0.5\varepsilon_0\omega\mathrm{Im}[\varepsilon(\omega)]E_{loc}^2$ [47,48]. Herein, the frequency ω and the extinction coefficient $\mathrm{Im}[\varepsilon(\omega)]$ is fixed. Based on results of M_{max}, it is known that the maximum light absorption in graphene is enhanced from 31 to 55 times with d decreasing from 2 nm to 1 nm. It indicates that in real experiments it is important to reduce the tip-sample distance to achieve high light absorption in sub samples.

The distribution of M_{loc} in the near-field region at $d = 1$ nm is depicted in Fig. 6. Here, $z = 0$ denotes the upper surface of the graphene monolayer with a thickness $t_g = 0.34$ nm. M_{loc} distribution on the x-z plane through the tip central axis is shown in Fig. 6 (a). It is noted that M_{max} in the gap region is much higher than that in the graphene with a ratio of ~187 which depends on the optical property of graphene [49]. The extremely high field enhancement region covers less than 10 nm on x-axis in the gap, formed by the joint effects of the gold tip and the monolayer graphene. Fig. 6 (b) is the x-y view of M_{loc} distribution at $z = 0.5$ nm in the tip-graphene gap. M_{loc} concentrates in a less than 10 nm region on y-axis. Fig. 6 (c) shows the x-y view of M_{loc} distribution under the graphene at $z = -0.35$ nm. It indicates that a considerable amount of light passes through the graphene layer and forms another concentrated spot, although M_{max} is relatively lower compared with that in the gap region. M_{loc} distribution in the monolayer graphene is shown in Fig. 6 (d). M_{loc} is lower in the center near the tip apex and higher in the outer circline region. The asymmetrical distribution with respect to the cross section at $y = 0$ is due to the side illumination. The asymmetrical distribution of M_{loc} similar as that of free-standing tip case indicates that the intensity enhancement in the monolayer graphene is induced directly by the optical enhancement around the gold tip apex.

Due to the tip-graphene induced significant optical enhancement, the localized heating resulting from the enhanced light absorption in the monolayer graphene could be utilized for thermal measurement, laser-assisted manufacturing, fabrication, and surface modification. [50,51] Such fundamental studies of monolayer graphene may perform as a guideline for other 2D materials. The fabrication process of graphene devices using PMMA as resist inevitably suffers from the contamination of a thin layer (1–2 nm) of PMMA adsorbed on the graphene surface [52]. Following the fabrication process, the thermal treatment method is usually used to eliminate the PMMA residue on the surface. In addition, the localized heating has also be used in controllable and localized surface annealing of graphene devices [19]. By using a heated AFM tip, tuning the reduction of graphene oxide (GO) to change the graphene properties has previously been achieved. In that work, the length of the trench induced by the AFM tip heating is approximately 25 nm. The scale of the induced hot spot in the graphene in our study is 40 nm (see Fig. 6d), which would cause localized heating in the small region and used for the property tuning of reduced GO. Besides, Raman spectroscopy is an effective tool for measuring local temperature of graphene and other 2D materials [53]. Such localized hot spot can be used to study the nanoscale thermal transport in graphene combined with the Raman method.

4. Conclusion

In summary, the tip-assisted photo-thermal conversion in silicon and monolayer graphene is numerically analyzed. The maximum optical enhancement around a free-standing gold tip is found dependent on the incident wavelength and angle. Compared with the results at 405, 532, 785 nm, the largest M_{max} near the tip apex occurs at 632 nm

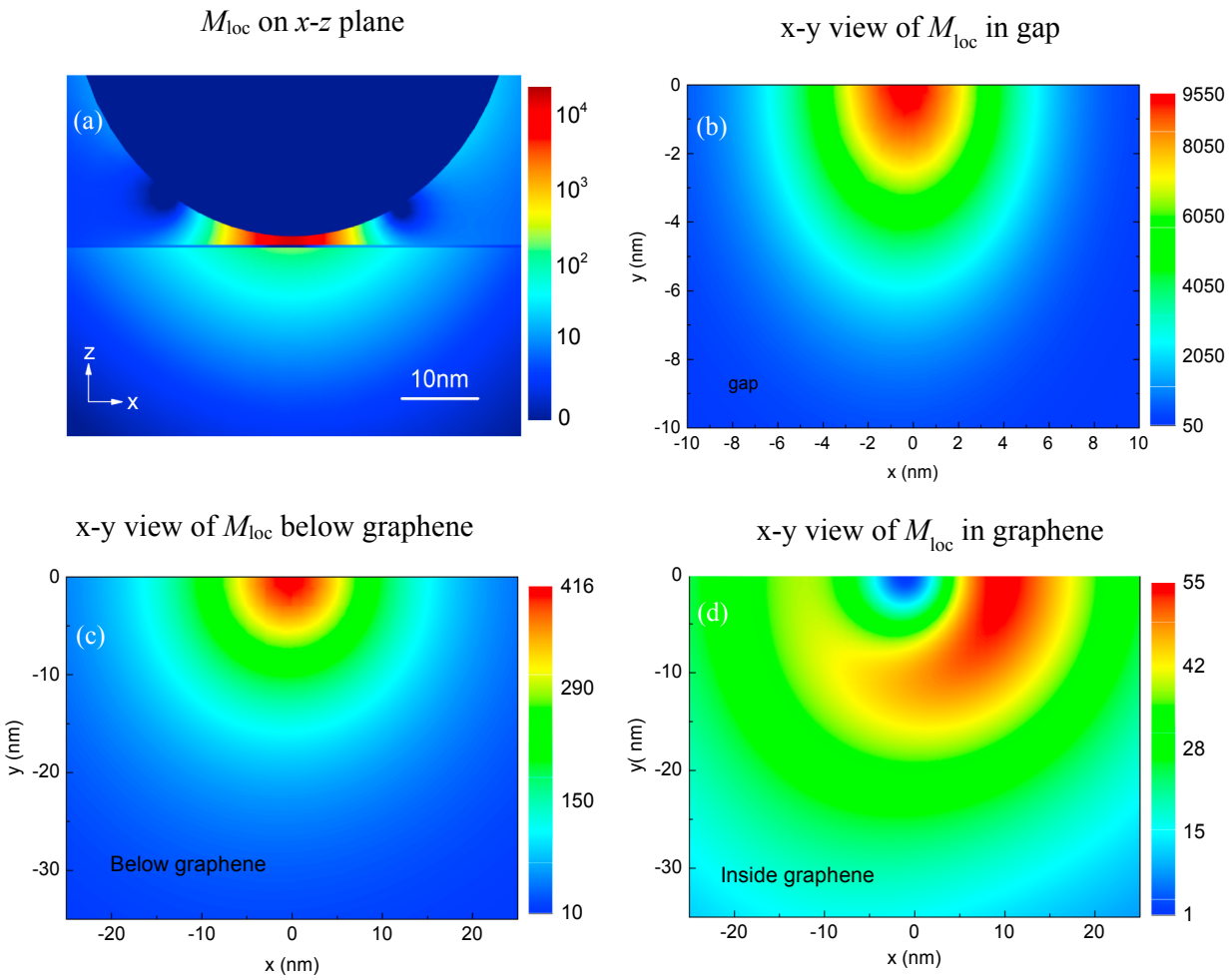

Fig. 6. (a) M_{loc} distribution (on a log scale) on *x-z* cross section through the tip cone axis. M_{loc} distribution from *x-y* view (b) in the gap region (above the monolayer graphene at z = 0.5 nm), (c) below the monolayer graphene (at z = -0.35 nm) and (d) in the monolayer graphene (at z = -0.1 nm).

with $\theta = 10^{\circ}$. For the tip-silicon configuration, M_{max} in the gap increases as the separation d is decreased and becomes the largest when the tip contacts the substrate. M_{loc} in the silicon is also larger for the contacting case. The generated heat source in the silicon has a resolution of ~6 nm laterally and ~2 nm vertically. The largest energy density reaches $\sim 2.98 \times 10^{15}\,\mathrm{W\,m^{-3}}$ at a moderate input moderate energy flux of $2 \times 10^{7}\,\mathrm{W\,m^{-2}}$, which is feasible for the subsurface modification, laser-assisted manufacturing and the study of ballistic thermal transport of silicon. As for 2D materials, metallic tip-graphene interaction is calculated. The light absorption in monolayer graphene can be enhanced by 55 times at separation $d = 1$ nm due to the near field effect. The tip-assisted localized energy absorption promises applications of surface cleaning, material properties tuning and thermal transport study for monolayer graphene and other 2D materials.

Acknowledgments

The financial support from the National Natural Science Foundation of China (No. 51576145) is gratefully acknowledged.

Appendix A. Supplementary material

Supplementary data to this article can be found online at https://doi.org/10.1016/j.applthermaleng.2018.11.050.

References

[1] D.K. Gramotnev, S.I. Bozhevolnyi, Nanofocusing of electromagnetic radiation, Nat. Photonics 8 (1) (2014) 13–22.
[2] T.-X. Huang, S.-C. Huang, M.-H. Li, Z.-C. Zeng, X. Wang, B. Ren, Tip-enhanced Raman spectroscopy: tip-related issues, Anal. Bioanal. Chem. 407 (27) (2015) 8177–8195.
[3] B.-S. Yeo, J. Stadler, T. Schmid, R. Zenobi, W. Zhang, Tip-enhanced Raman Spectroscopy-Its status, challenges and future directions, Chem. Phys. Lett. 472 (1) (2009) 1–13.
[4] E. Bailo, V. Deckert, Tip-enhanced Raman scattering, Chem. Soc. Rev. 37 (5) (2008) 921–930.
[5] X. Shi, Coca-López Ns, J. Janik, A. Hartschuh, Advances in tip-enhanced near-field raman microscopy using nanoantennas, Chem. Rev. 117 (7) (2017) 4945–4960.
[6] K.A. Willets, R.P. Van Duyne, Localized surface plasmon resonance spectroscopy and sensing, Annu. Rev. Phys. Chem. 58 (2007) 267–297.
[7] P. Liao, A. Wokaun, Lightning rod effect in surface enhanced Raman scattering, J. Chem. Phys. 76 (1) (1982) 751–752.
[8] P. Royer, D. Barchiesi, G. Lerondel, R. Bachelot, Near-field optical patterning and structuring based on local-field enhancement at the extremity of a metal tip, Philos. Trans.-Royal Soc. London Series A Mathematical Physical Eng. Sci. (2004) 821–842.
[9] L. Novotny, B. Hecht, Principles of nano-optics, Cambridge University Press, 2012.
[10] R.M. Roth, N.C. Panoiu, M.M. Adams, R.M. Osgood, C.C. Neacsu, M.B. Raschke, Resonant-plasmon field enhancement from asymmetrically illuminated conical metallic-probe tips, Opt. Exp. 14 (7) (2006) 2921–2931.
[11] C. Huber, A. Trugler, U. Hohenester, Y. Prior, W. Kautek, Optical near-field excitation at commercial scanning probe microscopy tips: a theoretical and experimental investigation, Phys. Chem. Chem. Phys. : PCCP. 16 (6) (2014) 2289–2296.
[12] A. Downes, D. Salter, A. Elfick, Simulations of tip-enhanced optical microscopy reveal atomic resolution, J. Microsc. 229 (2) (2008) 184–188.
[13] Z. Wang, B. Luk'Yanchuk, L. Li, P. Crouse, Z. Liu, G. Dearden, et al., Optical near-field distribution in an asymmetrically illuminated tip–sample system for laser/STM nanopatterning, Appl. Phys. A: Mater. Sci. Process. 89 (2) (2007) 363–368.
[14] C. Xiangwen, W. Xinwei, Near-field thermal transport in a nanotip under laser irradiation, Nanotechnology. 22 (7) (2011) 075204.

[15] A. Downes, D. Salter, A. Elfick, Heating effects in tip-enhanced optical microscopy, Opt Exp. 14 (12) (2006) 5216–5222.
[16] W. Zhang, T. Schmid, B.-S. Yeo, R. Zenobi, Near-field heating, annealing, and signal loss in tip-enhanced Raman spectroscopy, J. Phys. Chem. C. 112 (6) (2008) 2104–2108.
[17] A. Datta, X. Xu, Comparative study of optical near-field transducers for heat-assisted magnetic recording, Opt. Eng. 56 (12) (2017) 121906.
[18] Y. Yue, X. Chen, X. Wang, Noncontact sub-10 nm temperature measurement in near-field laser heating, Acs Nano. 5 (6) (2011) 4466–4475.
[19] Z. Wei, D. Wang, S. Kim, S.-Y. Kim, Y. Hu, M.K. Yakes, et al., Nanoscale tunable reduction of graphene oxide for graphene electronics, Science 328 (5984) (2010) 1373–1376.
[20] W. Zhang, X. Cui, O.J.F. Martin, Local field enhancement of an infinite conical metal tip illuminated by a focused beam, J. Raman Spectrosc. 40 (10) (2009) 1338–1342.
[21] E.D. Palik, Handbook of optical constants of solids, Academic press, 1998.
[22] D.E. Aspnes, A. Studna, Dielectric functions and optical parameters of si, ge, gap, gaas, gasb, inp, inas, and insb from 1.5 to 6.0 ev, Phys. Rev. B. 27 (2) (1983) 985.
[23] N. Behr, M.B. Raschke, Optical antenna properties of scanning probe tips: plasmonic light scattering, tip − sample coupling, and near-field enhancement, J. Phys. Chem. C. 112 (10) (2008) 3766–3773.
[24] R. Loudon, The propagation of electromagnetic energy through an absorbing dielectric, J. Phys. A: Gen. Phys. 3 (3) (1970) 233.
[25] Z.J. Coppens, W. Li, D.G. Walker, J.G. Valentine, Probing and controlling photothermal heat generation in plasmonic nanostructures, Nano Lett. 13 (3) (2013) 1023–1028.
[26] J. Hao, L. Zhou, M. Qiu, Nearly total absorption of light and heat generation by plasmonic metamaterials, Phys. Rev. B. 83 (16) (2011) 165107.
[27] G. Chen, Nonlocal and nonequilibrium heat conduction in the vicinity of nanoparticles, Trans.-Am. Soc. Mech. Eng. J. Heat Transfer. 118 (1996) 539–545.
[28] K.T. Regner, D.P. Sellan, Z. Su, C.H. Amon, A.J. McGaughey, J.A. Malen, Broadband phonon mean free path contributions to thermal conductivity measured using frequency domain thermoreflectance, Nat. Commun. 4 (2013) 1640.
[29] F. Yang, C. Dames, Mean free path spectra as a tool to understand thermal conductivity in bulk and nanostructures, Phys. Rev. B. 87 (3) (2013) 035437.
[30] Y. Ju, K. Goodson, Phonon scattering in silicon films with thickness of order 100 nm, Appl. Phys. Lett. 74 (20) (1999) 3005–3007.
[31] M.H. Kryder, E.C. Gage, T.W. McDaniel, W.A. Challener, R.E. Rottmayer, G. Ju, et al., Heat assisted magnetic recording, Proc. IEEE 96 (11) (2008) 1810–1835.
[32] S. Alimpiev, S. Nikiforov, V. Karavanskii, T. Minton, J. Sunner, On the mechanism of laser-induced desorption–ionization of organic compounds from etched silicon and carbon surfaces, J. Chem. Phys. 115 (4) (2001) 1891–1901.
[33] X. He, A. Datta, W. Nam, L.M. Traverso, X. Xu, Sub-diffraction limited writing based on laser induced periodic surface structures (LIPSS), Sci. Rep. 6 (2016) 35035.
[34] G.P. Zograf, M.I. Petrov, D.A. Zuev, P.A. Dmitriev, V.A. Milichko, S.V. Makarov, et al., Resonant nonplasmonic nanoparticles for efficient temperature-feedback optical heating, Nano Lett. 17 (5) (2017) 2945–2952.
[35] A. Carattino, M. Caldarola, M. Orrit, Gold nanoparticles as absolute nanothermometers, Nano Lett. 18 (2) (2018) 874–880.
[36] M. Aouassa, E. Mitsai, S. Syubaev, D. Pavlov, A. Zhizhchenko, I. Jadli, et al., Temperature-feedback direct laser reshaping of silicon nanostructures, Appl. Phys. Lett. 111 (24) (2017) 243103.
[37] S.V. Makarov, I.S. Sinev, V.A. Milichko, F.E. Komissarenko, D.A. Zuev, E.V. Ushakova, et al., Nanoscale generation of white light for ultrabroadband nanospectroscopy, Nano Lett. 18 (1) (2017) 535–539.
[38] H. Zhang, C. Hua, D. Ding, A.J. Minnich, Length dependent thermal conductivity measurements yield phonon mean free path spectra in nanostructures, Sci. Rep. 5 (2015).
[39] F.H. Koppens, D.E. Chang, F.J. García de Abajo, Graphene plasmonics: a platform for strong light–matter interactions, Nano Lett. 11 (8) (2011) 3370–3377.
[40] A. Grigorenko, M. Polini, K. Novoselov, Graphene plasmonics, Nat. Photonics 6 (11) (2012) 749–758.
[41] T. Low, P. Avouris, Graphene plasmonics for terahertz to mid-infrared applications, ACS Nano 8 (2) (2014) 1086–1101.
[42] B. Vasić, G. Isić, R. Gajić, Localized surface plasmon resonances in graphene ribbon arrays for sensing of dielectric environment at infrared frequencies, J. Appl. Phys. 113 (1) (2013) 013110.
[43] J. Lee, S. Shim, B. Kim, H.S. Shin, Surface-enhanced raman scattering of single-and few-layer graphene by the deposition of gold nanoparticles, Chem.-A Eur. J. 17 (8) (2011) 2381–2387.
[44] X. Ling, L. Xie, Y. Fang, H. Xu, H. Zhang, J. Kong, et al., Can graphene be used as a substrate for Raman enhancement? Nano Lett. 10 (2) (2009) 553–561.
[45] Q. Zhang, X. Li, M.M. Hossain, Y. Xue, J. Zhang, J. Song, et al., Graphene surface plasmons at the near-infrared optical regime, Sci. Rep. 4 (2014).
[46] B. Liu, C. Tang, J. Chen, Q. Wang, M. Pei, H. Tang, Dual-band light absorption enhancement of monolayer graphene from surface plasmon polaritons and magnetic dipole resonances in metamaterials, Opt. Exp. 25 (10) (2017) 12061–12068.
[47] Y. Cai, J. Zhu, Q.H. Liu, Tunable enhanced optical absorption of graphene using plasmonic perfect absorbers, Appl. Phys. Lett. 106 (4) (2015) 043105.
[48] X. Zhu, L. Shi, M.S. Schmidt, A. Boisen, O. Hansen, J. Zi, et al., Enhanced light–matter interactions in graphene-covered gold nanovoid arrays, Nano Lett. 13 (10) (2013) 4690–4696.
[49] R.R. Nair, P. Blake, A.N. Grigorenko, K.S. Novoselov, T.J. Booth, T. Stauber, et al., Fine structure constant defines visual transparency of graphene, Science 320 (5881) (2008) 1308-.
[50] Q.-Y. Li, W.-G. Ma, X. Zhang, Laser flash Raman spectroscopy method for characterizing thermal diffusivity of supported 2D nanomaterials, Int. J. Heat Mass Transf. 95 (2016) 956–963.
[51] Q.-Y. Li, K. Xia, J. Zhang, Y. Zhang, Q. Li, K. Takahashi, et al., Measurement of specific heat and thermal conductivity of supported and suspended graphene by a comprehensive Raman optothermal method, Nanoscale 9 (30) (2017) 10784–10793.
[52] Y.-C. Lin, C.-C. Lu, C.-H. Yeh, C. Jin, K. Suenaga, P.-W. Chiu, Graphene annealing: how clean can it be? Nano Lett. 12 (1) (2011) 414–419.
[53] S. Sullivan, A. Vallabhaneni, I. Kholmanov, X. Ruan, J. Murthy, L. Shi, Optical generation and detection of local nonequilibrium phonons in suspended graphene, Nano Lett. 17 (3) (2017) 2049–2056.